JGR Solid Earth

RESEARCH ARTICLE
10.1029/2018JB016642

Mantle Transition Zone Structure Beneath Northeast Asia From 2-D Triplicated Waveform Modeling: Implication for a Segmented Stagnant Slab

Yujing Lai[1,2], Ling Chen[1,2,3], Tao Wang[4], and Zhongwen Zhan[5]

[1]State Key Laboratory of Lithospheric Evolution, Institute of Geology and Geophysics, Chinese Academy of Sciences, Beijing, China, [2]College of Earth Sciences, University of Chinese Academy of Sciences, Beijing, China, [3]CAS Center for Excellence in Tibetan Plateau Earth Sciences, Beijing, China, [4]Institute of Geophysics and Geodynamics, School of Earth Sciences and Engineering, Nanjing University, Nanjing, China, [5]Seismological Laboratory, California Institute of Technology, Pasadena, California, USA

Key Points:
- The 2-D triplicated waveform modeling reveals fine-scale velocity structure of the Pacific stagnant slab
- High V_p/V_s ratios imply a hydrous and/or carbonated MTZ beneath Northeast Asia
- A low-velocity gap is detected within the stagnant slab, probably suggesting a deep origin of the Changbaishan intraplate volcanism

Supporting Information:
- Supporting Information S1

Correspondence to:
L. Chen and T. Wang,
lchen@mail.iggcas.ac.cn;
twang0630@nju.edu.cn

Citation:
Lai, Y., Chen, L., Wang, T., & Zhan, Z. (2019). Mantle transition zone structure beneath Northeast Asia from 2-D triplicated waveform modeling: Implication for a segmented stagnant slab. *Journal of Geophysical Research: Solid Earth*, *124*, 1871–1888. https://doi.org/10.1029/2018JB016642

Received 5 SEP 2018
Accepted 18 JAN 2019
Accepted article online 25 JAN 2019
Published online 16 FEB 2019

Abstract The structure of the mantle transition zone (MTZ) in subduction zones is essential for understanding subduction dynamics in the deep mantle and its surface responses. We constructed the P (V_p) and SH velocity (V_s) structure images of the MTZ beneath Northeast Asia based on two-dimensional (2-D) triplicated waveform modeling. In the upper MTZ, a normal V_p but 2.5% low V_s layer compared with IASP91 are required by the triplication data. In the lower MTZ, our results show a relatively higher-velocity layer (+2% V_p and −0.5% V_s compared to IASP91) with a thickness of ~140 km and length of ~1,200 km atop the 660-km discontinuity. Taking this anomaly as the stagnant slab and considering the plate convergence rate of 7–10 cm/year in the western Pacific region during the late Cenozoic, we deduced that the stagnant slab has a subduction age of less than 30 Ma. This suggests that the observed stagnancy of the slab in the MTZ beneath Northeast Asia may have occurred no earlier than the Early Oligocene. From the constraints derived individually on V_p and V_s structures, high V_p/V_s ratios are obtained for the entire MTZ beneath Northeast Asia, which may imply a water-rich and/or carbonated environment. Within the overall higher-velocity stagnant slab, a low-velocity anomaly was further detected, with a width of ~150 km, V_p and V_s reductions of 1% and 3% relative to IASP91. Such a gap may have provided a passage for hot deep mantle materials to penetrate through the thick slab and feed the Changbaishan volcano.

1. Introduction

The mantle transition zone (MTZ), a layer bounded by the 410- and 660-km discontinuities, is of great interest geodynamically and seismically, as being the crux in determining the exchange of materials and heat between the upper and lower mantle, as well as having marked water storage capacity jump at its boundaries. In Northeast Asia, the Pacific plate has been subducting along the Japan trench at a rate of 7–10 cm/year (Si et al., 2016) and has already reached the MTZ, interplayed with both the 410- and 660-km discontinuities in sequence and rendered uplift/depression of the two discontinuities, respectively. Due to the complex tectonics involving oceanic plate subduction and intraplate volcanism, the MTZ structure beneath Northeast Asia is rather heterogeneous. It has always been under the limelight and served as an ideal place to study the subduction dynamics and deep mantle processes as well as the associated geological phenomena on the surface. Although much progress has been made in recent years, a detailed and consistent understanding of the thermal state and chemical composition (i.e., water content) of the MTZ beneath Northeast Asia still eludes us.

Previous tomographic studies have revealed the high-velocity (high-V) Pacific plate subducting beneath Northeast Asia and provided the current slab morphology above, inside, and below the MTZ (e.g., Gorbatov & Kennett, 2003; Huang & Zhao, 2006; Li & van der Hilst, 2010). Specifically, the near-horizontal deflection of the Pacific subducted slab above the 660-km discontinuity was first detected from a travel time analysis by Okino et al. (1989), later imaged by van der Hilst et al. (1991, 1993) and Fukao et al. (1992, 2001) with the presence of stagnant slabs in the MTZ beneath Japan Sea, the northern part of Philippine Sea, and East China. These seismic travel time-based inversions have shed important light on the deep structure of Northeast Asia and delineated a rough picture of the subducted slabs. However, due to limited spatial resolution and contamination of complex caustic waveforms from the discontinuities (such as triplicated

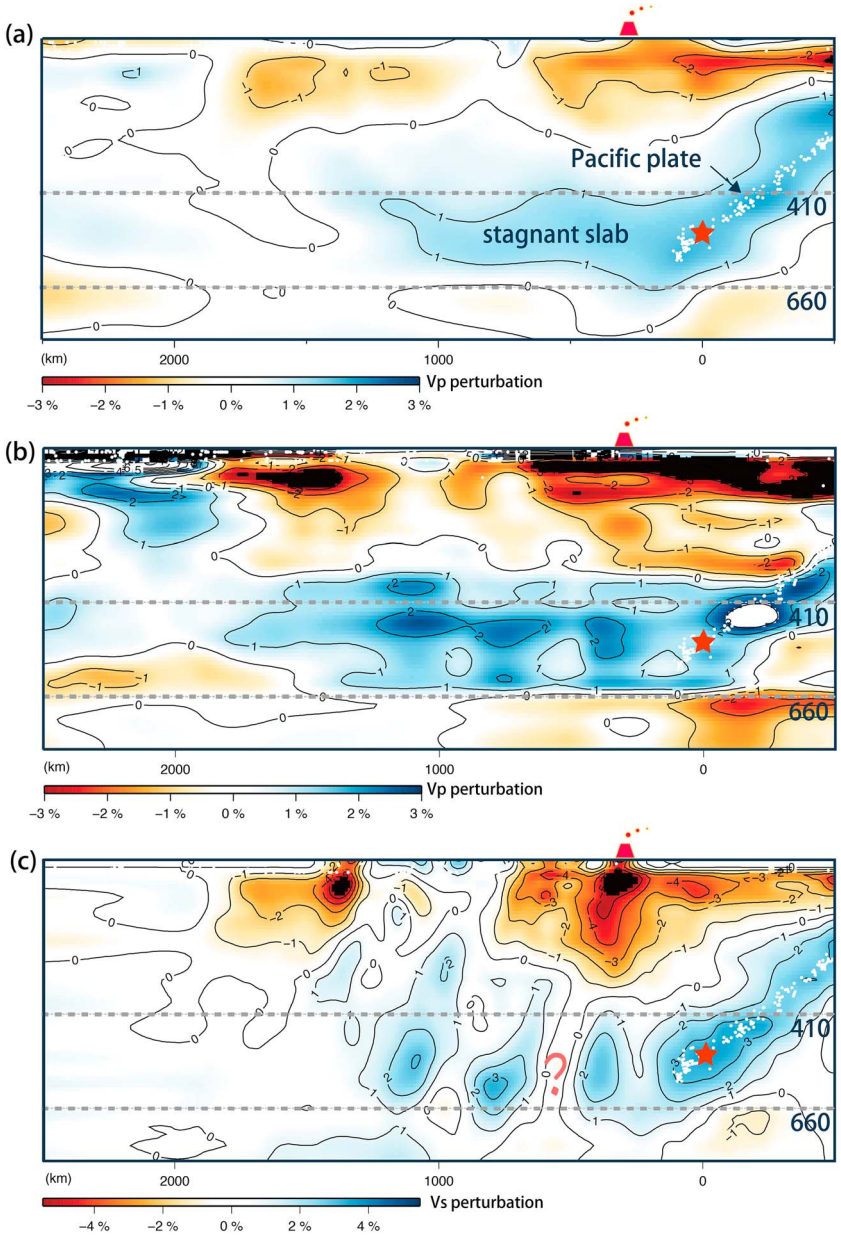

Figure 1. Three tomographic images along a profile crossing northeastern Asia (orange dashed line in Figure 2a). (a) *P* wave model gap_p4 (Fukao & Obayashi, 2013). (b) *P* wave model LLNL-G3Dv3 (Simmons et al., 2012). (c) *S* wave model NECESS (Tang et al., 2014). White dots show the earthquakes occurred during 1950–2016 within a 50-km distance from the profile (records from USGS), and red stars denote a deep earthquake 20080519 used in this study. Question mark indicates a possible low-*V* gap in the slab. The location of the Changbaishan volcano is marked on top of each panel.

waves), differences and controversies exist in the structural images of subducted slabs. For example, the lateral extent of the stagnant Pacific slab and its continuity beneath Northeast China remain contentious. Even along a same profile, tomographic results suggested various lengths of the stagnant slab, ranging from ~1,200 km (Figures 1a and 1c; Fukao & Obayashi, 2013; Tang et al., 2014) to both shorter (e.g., ~700–800 km; Chen & Pei, 2010; Li & van der Hilst, 2010) and longer lengths (e.g., ~1,800 km in Figure 1b; Simmons et al., 2012), with distinct slab structural features (Figure 1).

Moreover, the origin of the intraplate volcanism in Northeast Asia has not been well understood either. For example, many tomographic results showed a low-velocity (low-V) anomaly in the upper mantle and interpreted it to be the source area of the Changbaishan volcano, the most active one in Northeast China (e.g., Lei

& Zhao, 2005; Li & van der Hilst, 2010; Simmons et al., 2012; Takeuchi et al., 2014; Tang et al., 2014; Zhao et al., 2009). The vertical and horizontal extents of such a low-*V* anomaly vary among different studies (Figure 1). In some models (e.g., Lei & Zhao, 2005; Li & van der Hilst, 2010; Tang et al., 2014; Zhao et al., 2009), the low-*V* anomaly was imaged to extend down into the MTZ, while other models (e.g., Fukao & Obayashi, 2013; Huang & Zhao, 2006; Wei et al., 2012) suggested that the low-*V* anomaly is confined to the uppermost 200–300-km mantle. Recently, Tang et al. (2014) identified a low-*V* conduit penetrating through the stagnant slab in the MTZ and took it as evidence for a deeper origin of the Changbaishan volcanism from below the 660-km discontinuity. To fully understand the origin of the surface volcano and its relationship with the deep subduction dynamics, it is of great necessity to explore the detailed structure of the slab and the surrounding mantle especially in the MTZ.

The actual water content in the MTZ is another hotly debating topic. Water in deep Earth plays an important role on mantle dynamics due to its effect in modifying the melting relationships (e.g., Inoue, 1994) and rheological properties (e.g., Karato & Jung, 2003; Mei & Kohlstedt, 2000). Major minerals in the MTZ such as wadsleyite and ringwoodite can accommodate up to ~3 wt % of water (Kohlstedt et al., 1996), which is much higher than its upper and lower mantle counterparts. Seismic low-velocity zones (LVZs) detected above the 410-km discontinuity (e.g., Liu et al., 2016; Song et al., 2004; Tauzin et al., 2017) and below the 660-km discontinuity in various regions including Northeast Asia (Liu et al., 2016; Schmandt et al., 2014) were attributed to dehydration melting induced by water transport out of the MTZ. Studies of the inclusions in diamonds have also suggested an aqueous MTZ (e.g., Tschauner et al., 2018). However, the exact water content is under debate. Some researchers suggested that the MTZ beneath Northeast Asia is hydrous (0.2–0.4 wt %; Li et al., 2013; Ye et al., 2011) due to intensive hydration by ancient slab subduction and stagnation (Kuritani et al., 2011) through water transport into deep mantle (Ohtani et al., 2004; Song et al., 2007). More recently, Fei et al. (2017) argued that the MTZ should be nearly water-saturated (1–2 wt %) globally based on mantle viscosity fitting result. On the other hand, some researches believed that little water exists in the MTZ (e.g., Houser, 2016; Yoshino et al., 2008). For example, it is reported that only a dry model explains well the conductivity–depth profiles obtained from geoelectromagnetic studies (Yoshino et al., 2008). Green et al. (2010) also argued that the existence of deep earthquakes requires subducted slabs to bring only negligible (<100 ppm by weight) amount of water into the MTZ. To provide more effective constraints on the water content in the MTZ, more detailed information about its structure, thermal state, and composition variation are highly demanded.

In this study, we aimed to construct an accurate MTZ velocity model beneath Northeast Asia so as to gain a more comprehensive understanding of the subduction dynamics and explore the relevance between the intraplate vocalism and mantle process. We used seismic waveforms that are more sensitive to complex structures and seismic velocity variations compared to travel times. For example, Chen et al. (2007) focused on a strong secondary arrival of the SH wave train and detected a thin (~20 km), elongated low-*V* layer atop the slab in the Japan subduction zone, while such a structure can hardly be imaged with standard travel time tomographic techniques (Chen et al., 2007). Regional triplicated waveforms, which include multiple seismic phases associated with one discontinuity structure, sample the MTZ most extensively than any other wave types and interact strongly with the discontinuities in the MTZ. Triplicated waveform modeling can therefore serve as an effective tool in constraining the MTZ velocity structure. Some one-dimensional (1-D) triplicated waveform modeling studies have been conducted to investigate the MTZ structure in the western Pacific subduction zone, which all suggest a high-*V* layer in the MTZ with some local low-*V* anomalies (Li et al., 2013; Tajima et al., 2009; Tajima & Grand, 1995; Wang et al., 2006; Wang & Chen, 2009; Wang & Niu, 2010; Ye et al., 2011). However, large lateral structural variation in this region cannot be effectively constrained with only 1-D velocity structure models. Given that 3-D waveform modeling is rather computational expensive and time-consuming yet with low resolution (Wang et al., 2014), 2-D triplicated waveform modeling is likely the most feasible approach to obtain a robust model of the velocity structure in the MTZ.

Based on the above considerations, we applied the 2-D triplicated waveform modeling technique to both the broadband *P* and SH waveforms from three deep earthquakes recorded by dense Chinese Regional Seismic Network to constrain the structure of the MTZ and morphology of the stagnant slab beneath Northeast Asia. We introduced the method and data in sections 2 and 3 and analyzed the triplicated waveforms in detail in section 4. We constructed the velocity models and showed confirmable evidence for the slab morphology in

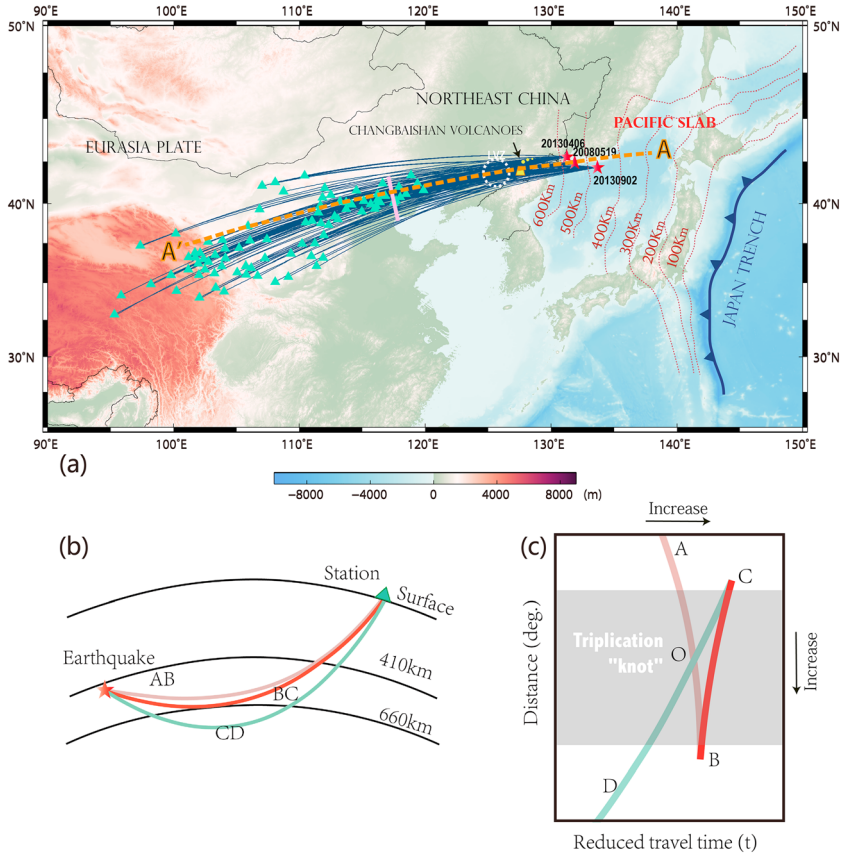

Figure 2. (a) Map showing the stations (green triangles) and three deep earthquakes (red stars) used in this study. Blue solid lines are great circle paths. The depth contours of the subducting Pacific slab (Hayes et al., 2012) are indicated by red dotted lines. Yellow triangle represents the Changbaishan volcano. Pink line indicates the western extension of the stagnant slab inferred from this study. White dashed circle shows the estimated location of a low-*V* zone in the MTZ described in section 4. (b and c) Schematic diagrams of the raypaths and travel time curves (branches) of the triplicated waves, including the AB branch—direct wave propagating above the 660-km discontinuity, the BC branch—wide-angle reflection off the discontinuity, and the CD branch—waves diving below the discontinuity. AB and CD intersect at point O. BOD mentioned latter means the intersection angle of OB and OD.

section 5. Lastly, we discussed thermal and compositional properties of the MTZ and dynamic mantle processes associated with the Pacific subduction.

2. Method

The 2-D seismic waveform modeling on both *P* and SH triplicated phases is used in our study to confine the MTZ structure. Regional *P* and *S* waves are termed as triplicated waves when every interaction with an increased velocity discontinuity (a positive velocity discontinuity or a discontinuity with a velocity increase; i.e., 660-km discontinuity) spawns three distinguishable branches (Figures 2b and 2c): waves propagating above the discontinuity (AB), waves reflecting at the discontinuity (BC), and waves refracting below the discontinuity (CD). Traveling over moderate distances of ~1,200–~3,000 km, triplicated waves from the 660-km discontinuity are clearly recorded in the seismograms, delivering abundant information for studying the MTZ velocity structure. We emphasized, as the previous study did (Li et al., 2013; Wang & Chen, 2009; Zhang et al., 2012), that we mainly focused on the relative travel times and amplitudes between the multiple phases instead of the absolute travel times and amplitudes, which can be influenced by structures outside the MTZ.

In contrast to previous studies using triplicated waveform modeling based on 1-D velocity structure, we simulated the 2-D regional elastic wavefield using the Spectrum-Element Method with the implementation of Komatitsch and Tromp (2002a, 2002b). We inserted the moment tensor source following the approach of

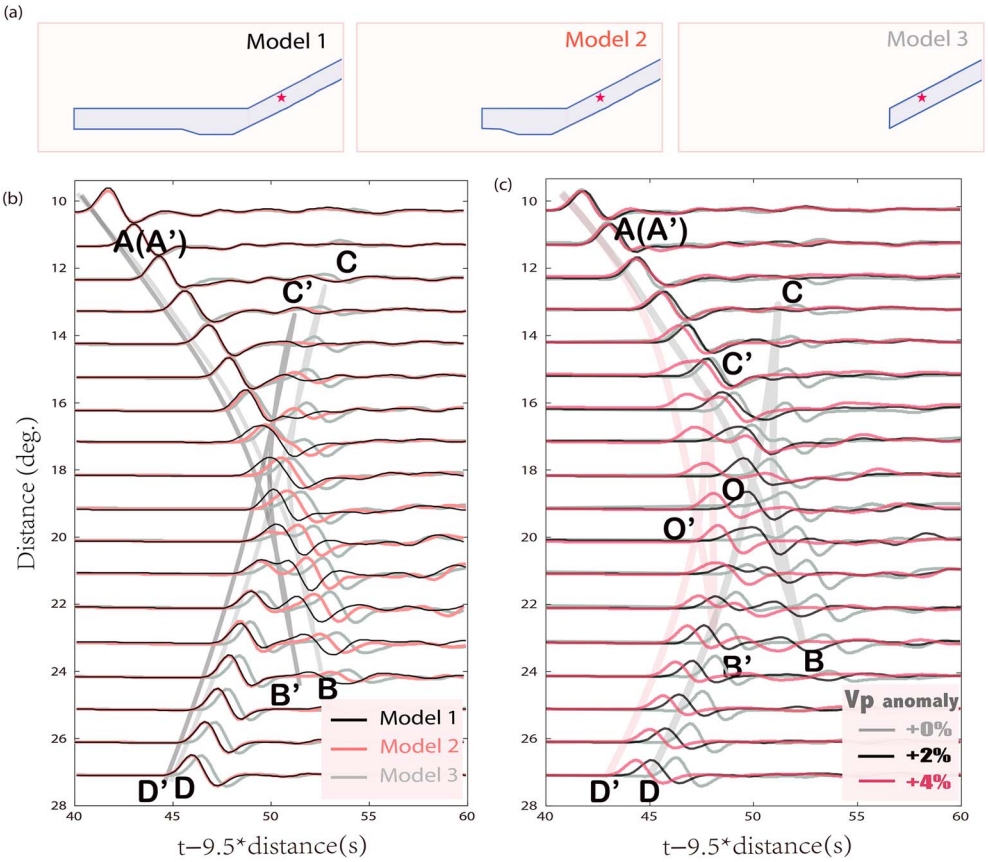

Figure 3. Slab models and corresponding synthetic triplicated waveforms. (a) Three different models with the stagnant slab length of 1,000, 500, and 0 km, respectively, and thickness of 140 km. The model includes an ~40-km depression at the bottoming part of the slab when it reaches the 660-km discontinuity. The thickness of the downgoing subducting slab is 90 km. The red stars indicate the location of the modeled earthquake with a focal depth of 459 km. Stations are all located on the surface to the left of the source. (b) Calculated synthetic triplicated *P* waveforms. Black, red, and gray lines correspond to the three models 1–3 in (a), respectively. The V_p anomaly for the slab is +2%. Light and dark gray lines AB (A′B′), BC (B′C′), and CD (C′D′) mark the arrival times of the three triplicated branches for model 3 and model 1, which are plotted by picking the onset time of each phases. (c) Calculated synthetic triplicated *P* waveforms based on model 2 in (a), with three magnitudes of V_p anomalies for the stagnant slab +0%, +2%, and +4% (gray, black, and red).

Li et al. (2014). To resolve the synthetics with high-frequency content of up to 0.8 Hz, we set the Spectrum-Element Method grid to 2 km throughout the entire domain, and the time step to 0.005 and 0.01 s for *P* and SH wave, respectively, which transfers to 1,750 × 1,500 grid points (3,500 km in the horizontal and 3,000 km in the vertical). The source was placed at least 400 km away from the right boundary and 1,000 km above the bottom to avoid spurious reflections. On 480 processors of a modern PC cluster (Xeon E5 CPU, Tianhe-2 High-Performance Center; http://en.nscc-gz.cn/Product/HighPerformanceComputingService/ServiceCharacteristics.html), it roughly takes 30 min for each simulation.

To get a first impression of how sensitive the triplicated waveforms are on slab morphology and velocity anomaly, we performed a series of synthetic tests (Figure 3). Our results show that triplicated waveforms begin to diverge at distances over 12° (Figure 3b) among models with different lengths of the stagnant slab (Figure 3a). In the distance range of 12°–21°, travel times of the triplication become earlier and the cusp points (B and C) appear at larger distances as the length of the stagnant slab increases. It suggests that the existence of a high-*V* stagnant slab results in a downward shifted BC branch. At distances larger than 21°, the CD branches for the two models with longer slabs (models 1 and 2) appear similar, whereas that without the stagnant flat slab (model 3) exhibits a distinctive feature with systematic delayed travel times at the same distances range (Figure 3b). We further changed the magnitude of the velocity anomaly of the slab in model 2 and investigated its influence (Figure 3c). Synthetic waveforms differ insignificantly at small distances

(<15°). From 15° to 27°, the larger the magnitude of the velocity anomaly is, the more substantial advancing the AB and CD branches appear, along with a shrinking of the BOD (Figure 3c). These synthetic tests indicate that the triplicated waveforms are very sensitive to the MTZ velocity structure especially the stagnant slab itself, and thus can be used to effectively constrain the corresponding structure beneath Northeast Asia.

3. Data

We collected broadband seismic waveforms recorded by the dense Chinese Regional Seismic Network established since 2007 (Zheng et al., 2010). Three deep earthquakes with simple source time function and high signal-to-noise ratio records have been selected (Table S1). For event 20080519, we used *P* and SH waveform data from the same 38 stations to ensure a tight constraint on both kinds of wave velocity in the MTZ of Northeast Asia. For events 20130902 and 20130406, we deleted some SH wave records with low signal-to-noise ratio, while the remaining records still exhibit clear triplication patterns.

The selected three events are closely located near the China-Russia border region, sampling mostly the stagnant part of the subducted Pacific slab (Figure 2a). All the events are deeper than 410 km, so the triplications of the 660-km discontinuity are free of interference from those generated at shallow upper mantle discontinuities. Event 20080519 with M_w5.9 is the main earthquake we used in constructing our velocity model, which produced high signal-to-noise ratio *P* and SH waveforms. We adopted the focal depth of 519 km relocated by Li et al. (2013) from minimizing the residual of differential time of pP-*P* in teleseismic records relative to IASP91 (Kennett & Engdahl, 1991; Table S1). Event 20130902 with M_w5.7 is a shallower earthquake with the focal depth of 454.7 km (global CMT catalog). We relocated the focal depth to 459 ± 3 km by using 20 nearby stations (within 8°) with the CAP (cut and paste) method (Zhu & Helmberger, 1996). Event 20130406 with M_w5.8 is the deepest one, with the focal depth of 570 km determined by Li et al. (2015). For all the events, we used global CMT solution as the focal mechanism to calculate the synthetics.

The stations used in this study are narrowly distributed in the azimuthal range of 262° to 268° (Figure 2a and Table S2), which helps to reduce the influence of the lateral velocity variation and increase the accuracy of our 2-D modeling. We first removed the instrumental response and applied band-pass filters of 0.05–0.8 and 0.05–0.45 Hz to vertical and transversal displacements, respectively. Seismic profiles of all three events show clear three triplicated branches (AB, BC, CD) within the distance of 10°–28°.

4. Major Features of the Triplicated Waveforms

We will discuss the general features of the triplicated waveforms in this section, mainly focusing on the emerging, vanishing, and intersecting distances of the AB and CD branches as well as the relative times between successive phases. In order to get a primary impression of the triplication pattern, we calculated the synthetic waveforms based on model IASP91 and compared them with the observations.

4.1. Major Features of *P* Waves

Compared with synthetic waveforms, the observations exhibit different triplication features in many ways (Figure 4). For event 20080519, the separation between the AB and CD branch at distances between 18° and 22° is generally smaller than that of the synthetic waveforms with the relative travel time difference of ~1.5–2 s. Additionally, the vanishing distances of the AB branch and the emerging distances of the CD branch are larger than those in the synthetics. The intersection point O also differs a lot. Such discrepancies between the observation and synthetics are also reflected for event 20130902 and event 20130406. For example, at distance at 19°–23°, the separation between the AB and the CD branch in the observation is smaller than that of the synthetics and the BC branch appears at greater distances in the observation for event 20130902 (Figure S1). To decrease the separation between two synthetic branches, it is required that either the AB branch becomes faster or the CD branch slower, indicating either a high-V_p anomaly in the lower MTZ or a low-V_p anomaly beneath the 660-km discontinuity. In the synthetic tests (Figure 3c), the existence of a high-V_p stagnant slab can render a narrow BOD, which may suggest the existence of a high-V_p anomaly in the bottom of the MTZ.

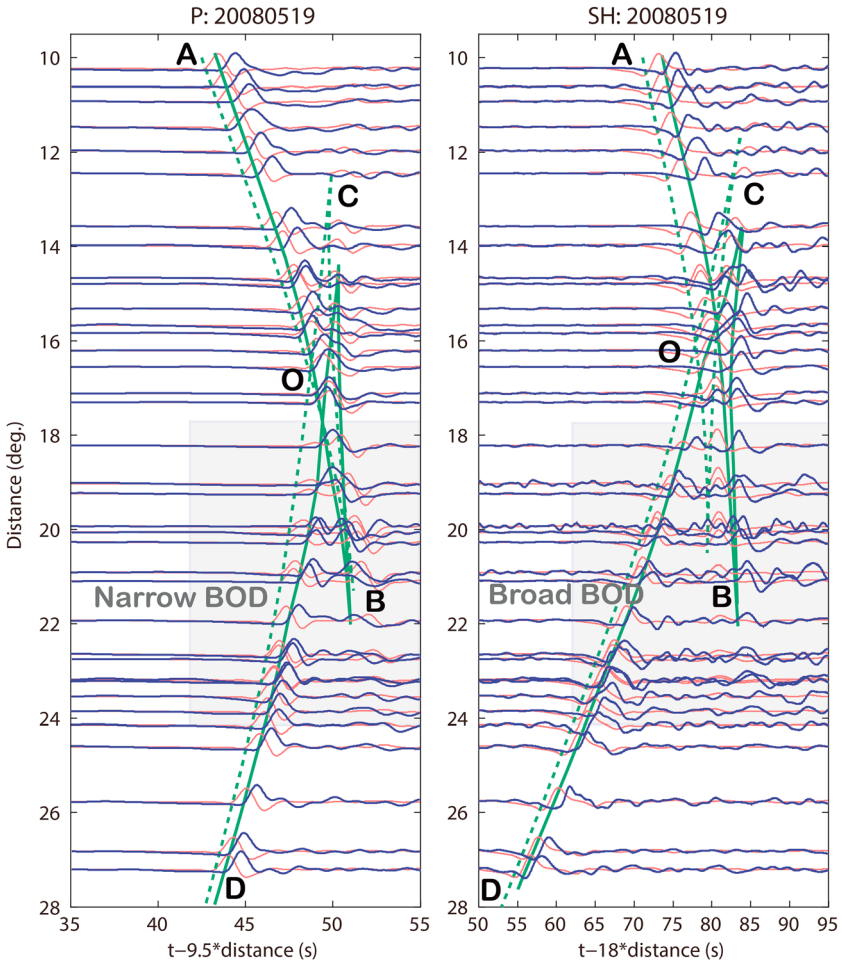

Figure 4. Comparison of the observed (solid blue line) and synthetic (solid red line; IASP91 model) vertical and tangential waveforms for event 20080519. Solid green and dashed green lines are their travel times by picking the onsets of the waveforms of each phases (same for travel times plotted in later figures), respectively. Broad and narrow BOD region are shaded in light gray.

4.2. Major Features of SH Waves

Compared with the synthetic waveforms (Figure 4), the observations have larger vanishing and emerging distances for the AB and CD branches, which is in accordance with *P* waves. However, we observed a larger separation between AB and CD branches at greater distances (distances over point O), in contrast to a small separation of the two branches in *P* waves (compare the left and right panels in Figure 4). Such a feature is clearly present in the waveforms from all the events. We termed it as a broader (narrow) BOD region for SH (*P*) triplicated waves after Li et al. (2013). Another feature worthy being noted is that the travel time curve of the observed AB branch of SH waves is generally in parallel with that of the synthetics, while they intersect in the case of *P* waves (Figure 4). This implies that the velocity gradient of *P* wave is larger than that of SH wave, and thus, a faster V_p or slower V_s anomaly is required in the lower MTZ. We will further discuss this feature in section 5.

5. Construction of the 2-D Slab Model

5.1. *P* Wave Triplication Modeling

To better match the observations, we tried to establish an initial velocity model to reflect the structural feature of the target region. Various previous tomographic models (Fukao & Obayashi, 2013; Huang & Zhao, 2006; Tang et al., 2014) have revealed a stagnancy of the subducted slab above the 660-km discontinuity

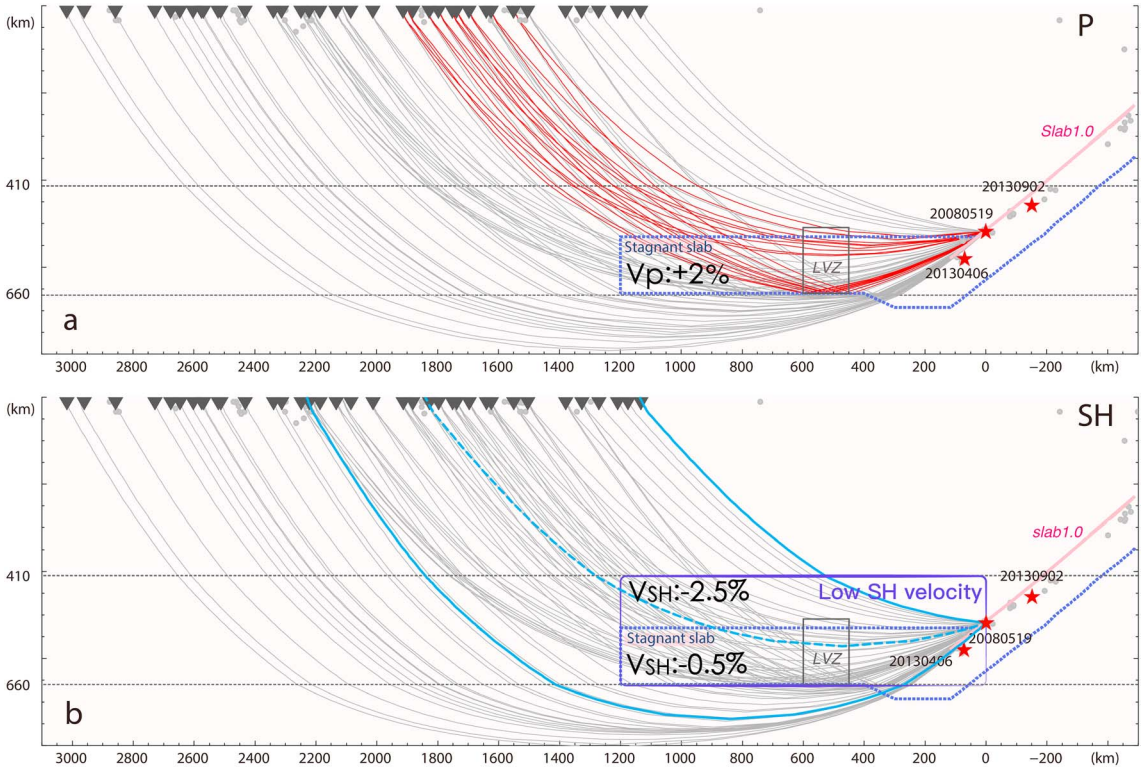

Figure 5. Cross section showing the slab model derived in this study (dotted purple lines) and great circle raypaths (gray, red, and cyan lines) of the triplicated waves for event 20080519 (back azimuth ~265°) calculated via TauP (Crotwell et al., 1999) using IASP91. The differences in raypaths among 2-D, 1-D, and other near-source structures are small as shown in Figures S4, S5, and S6 in which the 2D ray paths were computed using the fast marching method (de Kool et al., 2006). Solid pink line, adopted from model slab 1.0 (Hayes et al., 2012), denotes the upper boundary of the dipping part of the subducted Pacific slab. Gray dots show the earthquakes occurred during 1950–2016 within a 50-km distance from the profile (records from USGS), and red stars denote the three events used in this study. The origin of the *x* axis is set at the horizontal location of event 20080519 for convenience. The epicenter distances for the three raypaths (solid and dashed cyan thick lines) in (b) are 10.92°, 16.55°, and 20.27°, respectively. Red lines in (a) represent the records with obvious travel time delays.

beneath Northeastern Asia. The features of the *P* wave triplicated waveforms analyzed in section 4 also suggest the possible existence of a high-*V* anomaly in the lower MTZ. It is thus necessary to add a high-*V* slab anomaly in the MTZ in the regional velocity model. For modeling purposes, we first specified our initial model with a uniform *P* wave velocity anomaly, representing a subducted slab dipping in the shallow upper mantle and flat lying above the 660-km discontinuity, superposed on the IASP91 model (Figure 5a).

For the dipping slab, we constructed the upper boundary from slab1.0 model (Hayes et al., 2012) and then assumed a dip angle of ~29° and a slab thickness of 90 km (Zhao et al., 1994). It should be noted that since all the events used in this study are located near the base of the inclined part of the slab, the triplicated waves sample mostly the stagnant part. Thus, the velocity structure of the inclined part of the slab has little influence on the forward modeling performance.

For the stagnant slab, we set its thickness to be 140 km after Li et al. (2013), which is thicker than the initial subducted part due to the buckling and piling-up effect at the 660-km discontinuity, which is mainly caused by the viscosity increase around the boundary as demonstrated in geodynamic and seismic studies (e.g., Li & Yuen, 2014; Tosi et al., 2013). Given the smearing effect and limited vertical resolution, it is understandable that tomographic models often show a much larger thickness of the stagnant slab, which could even fill up the whole MTZ. We also set an ~40-km depression of the 660-km discontinuity as illustrated by images of receiver functions (Liu et al., 2015) for the bottoming part of the subducted slab along our profile (Figure 5a).

We first tested our initial model by *P* wave triplicated waveform modeling for all the three events and then further verified and refined our model by *S* wave triplicated waveform modeling (next section). The recent two tomographic studies (Fukao & Obayashi, 2013; Tang et al., 2014) report ~+1% and ~+1.5% *P* wave velocity anomaly for the stagnant and downgoing slab, respectively, which are typically smaller than the results

Table 1
Information of Different Synthetic Models

Model Description			
Slab Length (km)	*P* Wave Perturbation	Synthetic Figure	Remarks
400	+1%	Figure S2a	
	+2%	Figure 6a	
	+3%	Figure 6b	
800	+1%	Figure S2b	
	+2%	Figure S3a	
	+3%	Figure S3b	
1200	+1%	Figure S2c	
	+2%	Figure 6c	Initial model
	+3%	Figure 6d	
Initial model with low-V_p gap		Figures 6f–6h	Preferred V_p model
S model shown in Figure 5b		Figures 8b, 8d, and S10	Preferred V_s model

of ~3–5% from previous waveform modeling studies for the dipping part of the subducted slab (Chen et al., 2007; Ding & Grand, 1994; Zhan et al., 2014). We also noticed that in these two recent tomographic models, the stagnant slab has a smaller velocity anomaly than the dipping part. Thus, in our study, we tested *P* velocity anomalies of +1%, +2%, and +3% for the stagnant slab, and+3% for the dipping slab, to find out the best velocity model. To compensate for the *P* and *S* time residuals at shorter distances (Figure 4), which mainly result from the shallow upper mantle structure, we followed the approach similar to Tajima and Grand (1998) and Li et al. (2013) and modified the velocity structure above the 410-km discontinuity after Fukao (1977) to improve the consistency in absolute times.

We tested a series of models (Table 1) with different lengths and velocity anomalies of the stagnant slab to search for the best fitting to the observations. In general, the synthetics calculated from models with a stagnant slab extension of 400 km (Figures 6a, 6b, and S2a) have larger relative time differences (1.5~2 s) between the CD and AB branches at 19°–22°, which indicates higher velocities in the sampling region roughly at the depth of 520–660 km. This involves two possibilities: the first one is to increase the magnitude of high-V_p anomaly of the stagnant slab. This option fails because a high-V_p anomaly up to 5% still cannot fit the observed AB branch at 19°–22°, and it results in the CD branch arriving 1.5 s earlier at 18°–28° compared to the real data (Figure S3c). The second option is to increase the length of the stagnant slab. Modeling results (Figures 6c, 6d, and S2) showed that the stagnant slab model with a length of 1,200 km and a velocity anomaly of +2% improves the fitting performance, in which the differences of the relative times between the CD and AB branches are less than 0.2 s (Figure 6c). Such a 1,200-km extension of the slab is also consistent with two recent tomographic results (Fukao & Obayashi, 2013; Tang et al., 2014). Therefore, we took the stagnant slab model with a 1,200-km length and +2% *P* wave velocity anomaly as our base model for further model refinement.

For event 20080519, comparing the data with the synthetics from the above base model, we observed a noticeable travel time delay of ~1 s at 15°–19° for the AB and BC branches (dashed gray box in Figure 6c). For event 20130902, similar time delays were also observed, though in a different epicenter distance range of 16°–24° (dashed gray boxes in Figure 6e). We inferred from the intersection of the raypaths for these two events (Figures S7 and S8) that a low-V_p anomaly in the MTZ, but not in the shallow upper mantle, is required to explain the larger travel times. The upper boundary of the low-V_p anomaly is estimated to be around 510 km by considering the turning depths of the raypaths at a minimum distance with such travel time delays. The horizontal range is determined by the turning points of both AB and BC branches with slow arrivals (red lines in Figure 5a). We have also tested models with a low-V_p anomaly at other locations (Figure S7) and they all showed worse performances (Figure S8). Overall, our preferred model for *P* wave is the base model with the stagnant slab plus a low-V_p anomaly (−1%) of ~150-km wide and ~160-km high located above the 660-km discontinuity (Figure 5a). Synthetics based on the preferred model can well explain the data for all the three events (Figures 6f–6h). Comparison of waveform cross correlations between observations and synthetics from our final model, IASP91, and a recent tomographic model (Fukao & Obayashi, 2013) shows a noticeably improvement of our model in fitting the observations (Figure 7).

5.2. SH Wave Triplication Modeling

We first tested the *S* wave velocity model calculated from the *P* wave velocity model built in section 5.1 (Figure 5a) using a scaling factor f = dlnVs/dlnVp = 1.0, 1.5, and 2.0, where dlnVp and dlnVs refer to the fractional velocity perturbations with respect to IASP91; f value was adopted from Chen et al. (2007). All the three triplicated branches in synthetic waveforms show smaller travel times compared to the data for both event 20080519 and event 20130902 (Figures 8a, 8c, and S9), suggesting lower SH velocities especially in the MTZ as sampled by all the triplicated waves. In addition, the broad BOD demonstrated in Figures 4b and S1 show that time residuals between the AB and the CD branches are larger than those calculated from the IASP91 global model, which may also require a MTZ with low SH velocities (compared to IASP91) to

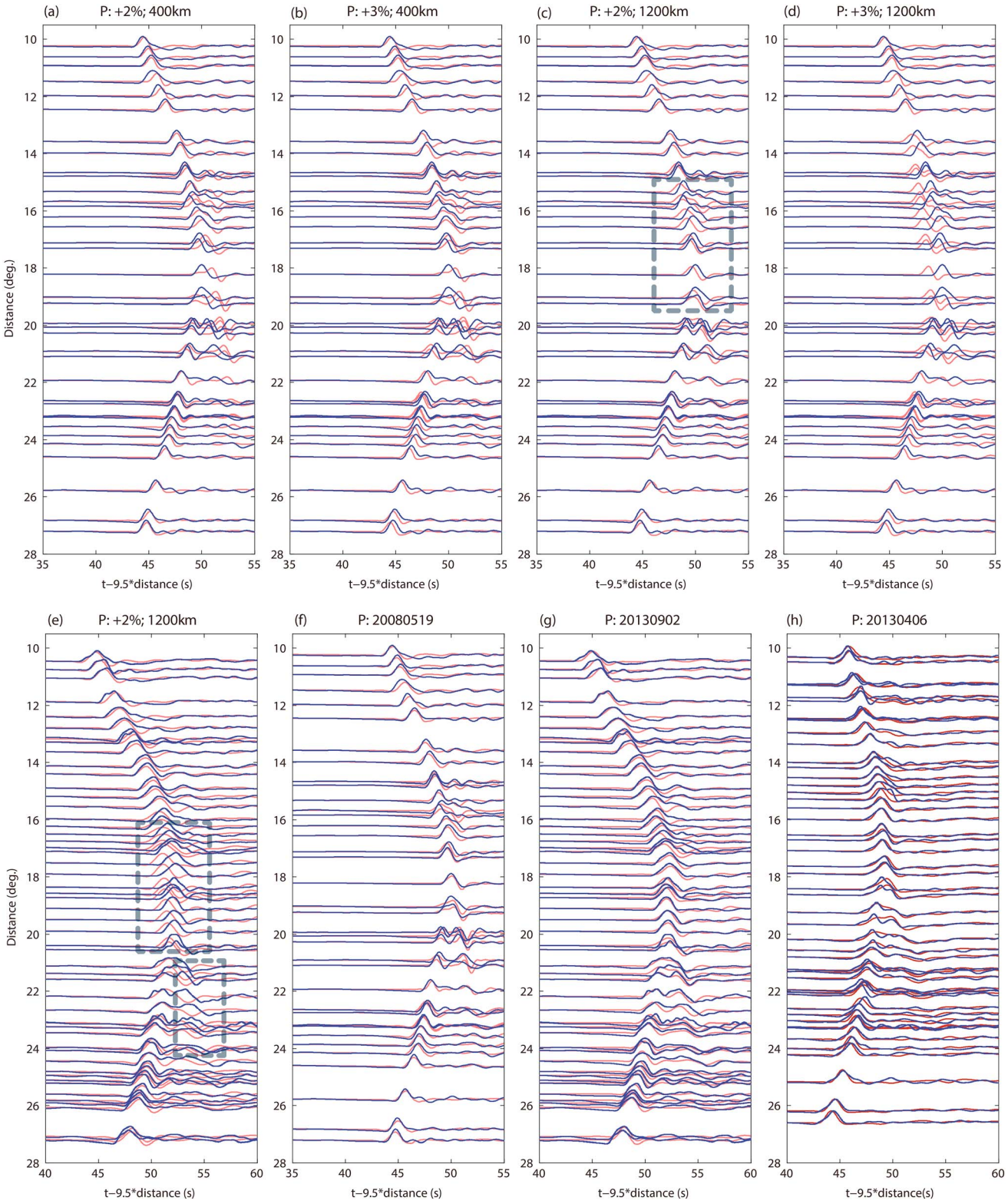

Figure 6. Comparisons of synthetic *P* waveforms (red lines) with observations (blue lines) for the three events 20080519, 20130902, and 20130406. Synthetics from (a–d) different stagnant slab models for event 20080519 and (e) from one model for event 20130902. The magnitude of velocity anomaly and length of the stagnant slab adopted in synthetic calculation are given on top of each panel. (f–h) Synthetics calculated from our preferred slab model (Figure 5a) for the three events. Dashed boxes show misfit between observation and synthetics calculated by corresponding model.

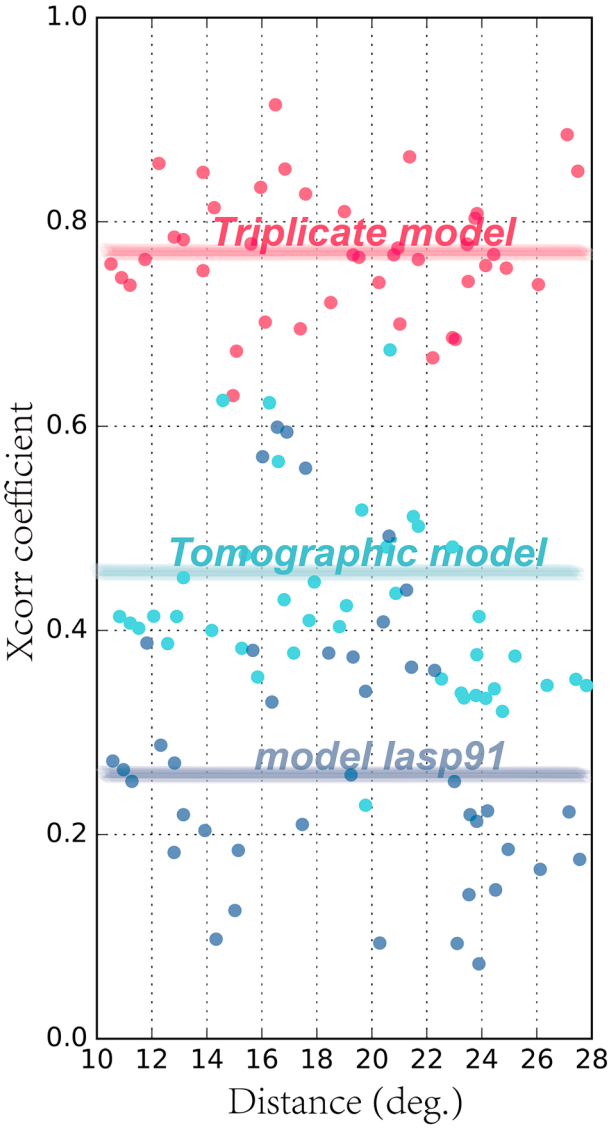

Figure 7. Comparison of the triplicated *P* waveform cross correlations between observations and synthetics calculated from IASP91, a tomographic model (Fukao & Obayashi, 2013) and our preferred model (red) on event 20130406. Circles represent the cross-correlation values at individual stations. Thick solid lines indicate the average values of the cross correlations for the three models, in which the red one represents our preferred triplicate model.

reconcile the larger travel times of the AB branch (broad BOD). To gain further insight into the lateral variations of the MTZ structure, we hand-picked the first SH arrival time at each distance and calculated the time residuals between the data and synthetics for event 20080519 and event 20130902 (Figure 9). We found that travel time residuals at the middle distance ranges (e.g., dashed cyan line in Figure 5b) are much larger than those at smaller and larger distances (e.g., solid cyan line in Figure 5b), and the time residuals are more than 2 times larger at distances in the shaded light red and shaded blue boxes (Figure 9). The raypath with the largest time residual for event 20080519 is shown as the dashed cyan line in Figure 5b. According to the raypath distribution (Figure 5b) and the *P* wave velocity model (Figure 5a), we inferred that such a time residual pattern of SH waves is also caused by a much lower SH velocity zone in the overall slow MTZ: the AB branches at smaller distances and CD branches at larger distances only sample the slow MTZ limitedly, resulting in minor time residuals; the AB phases at middle distances sample a large portion of the lower SH velocity zone, which gives rise to greater time residuals.

Based on the above analysis, we modified the *S* wave velocity model to fit the SH triplicated waveforms of the two events 20080519 and 20130902 (Figures 8b and 8d) and also those of the third event 20130406 (Figure S10). Consistent with our *P* wave velocity model, the final SH wave velocity model (Figure 5b) also contains a stagnant slab of 140-km thick and 1,200-km long lying above the 660-km discontinuity with relatively high velocities (+2% compared to the upper MTZ). It is intriguing that the MTZ at the stagnant slab region has a relatively slow SH velocity, with −2.5% in the upper MTZ and −0.5% within the stagnant slab compared to IASP91, contrasting to the *P* wave velocity model. To improve the fitness to the data, it is also required that a low-V_s anomaly is present inside the stagnant slab in the SH velocity model, with a velocity perturbation of −3% relative to IASP91 (Figure 5b).

6. Discussion

From triplication modeling for both *P* and SH waves from three deep earthquakes with nearly identical station-event geometries, we derived three major features of the MTZ velocity structure beneath Northeast Asia (Figure 10). First, there is a relatively high-velocity layer compared with ambient mantle lying atop the 660-km discontinuity with a thickness of ~140 km and a length of ~1,200 km, which we interpret to represent the stagnant Pacific slab in the MTZ. Second, compared to +2% V_p anomaly for the stagnant slab and the normal V_p structure above the slab with respect to the global IASP91 model, the SH velocity in the MTZ is consistently lower, with a magnitude of −0.5% in the stagnant slab and −2.5% in the upper MTZ. Third, a low-*V* anomaly for both *P* and SH waves is present within the stagnant slab, located horizontally at the westward vicinity of Changbaishan volcano (Figures 2a and 9). These features of *P* and SH wave velocity structure provide important constraints on the compositional and thermal properties of the stagnant slab and the MTZ as a whole.

6.1. Stagnant Slab in the MTZ

Slab stagnancy is a phenomenon commonly observed beneath subduction zones around the western Pacific rim and Mediterranean at depths above, across or below the 660-km discontinuity (Fukao et al., 2001; Fukao & Obayashi, 2013). The presence of a high-velocity stagnant slab beneath Northeast Asia has been revealed by many tomographic studies (e.g., Gorbatov & Kennett, 2003; Huang & Zhao, 2006; Li & van der Hilst, 2010). However, due to the smoothing effect and limited resolution, the boundary between the slab and

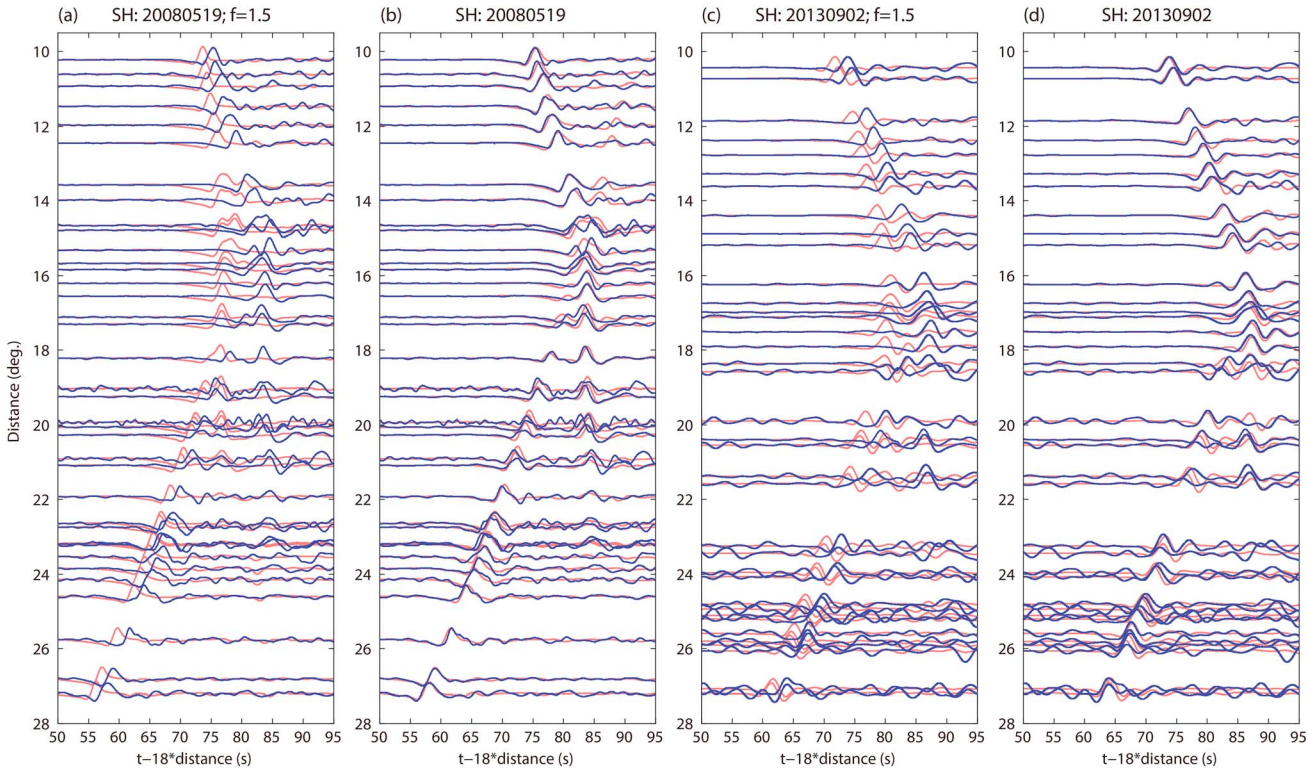

Figure 8. Seismic profiles of the SH waves for two events 20080519 and 20130902. The syntheses (red) of (a) and (c) are computed from the SH velocity model which is obtained by using a scaling factor f = dlnVs/dlnVp = 1.5 from the preferred P velocity model (Figure 5a), while the syntheses of (b) and (d) are computed from our preferred SH velocity model (Figure 5b). Blue lines are observations.

ambient mantle is quite obscure, making it difficult to determine a clear morphology of the stagnant slab. For most tomography results, the imaged stagnant slab is lying in the MTZ, but with various slab thickness, length, and shape (Li & van der Hilst, 2010; Si et al., 2016; Wei et al., 2012). Previous 1-D triplicated waveform modeling (e.g., Li et al., 2013; Tajima & Grand, 1998; Wang & Chen, 2009), which only yielded averaged 1-D models without information of lateral structural variations, is hard to characterize the heterogeneous subduction zone structure. In our 2-D triplication study, the modeling results reveal a consistent feature of a relatively high-velocity slab with a western extension of ~1,200 km just atop the 660-km discontinuity. This feature is robust, since for both P and SH waveforms, it renders the same relative times between the AB and CD branches compared with the observations from all the three events of different focal depths, especially when we consider the unique sensitivity of the triplication on the slab length as illustrated in Figure 3b. The ~1,200-km length of the stagnant slab derived in this study can be used to constrain the subduction history. If we consider a plate convergence rate of 7–10 cm/year in the western Pacific region (Si et al., 2016), the subduction age of the stagnant slab can be estimated to be ~28 Ma (stagnant + subducted (oblique): $(1.2\times10^6 + 7.6\times10^5$ m)/(0.07 m/year)~28 Ma). This is consistent with the age analysis in Liu et al. (2017), implying that the present stagnancy in the MTZ beneath Northeast Asia may have occurred no earlier than the Early Oligocene, and thus is the Pacific slab rather than the ancient Izanagi slab, which may have already collapsed into the lower mantle.

6.2. Water- and Carbon-Related Melt Low SH Velocity in MTZ

In contrast to a normal P wave velocity (+2% for the stagnant slab) structure in the MTZ, the SH wave velocity is quite low compared with model IASP91 with −2.5% in upper MTZ and −0.5% in the stagnant slab. The V_p/V_s ratio of the upper MTZ and the stagnant slab part is ~1.89 and ~1.87 respectively, which are ~2.7% higher than the average values of 1.84 and 1.82 from model IASP91. Such a discrepancy between P and SH velocity model has been directly reflected by the narrow and broad BOD, respectively, at larger distances in P and SH waves (Figures 4 and S1). Previous 1-D waveforms modeling studies in Northeast Asia (e.g., Li

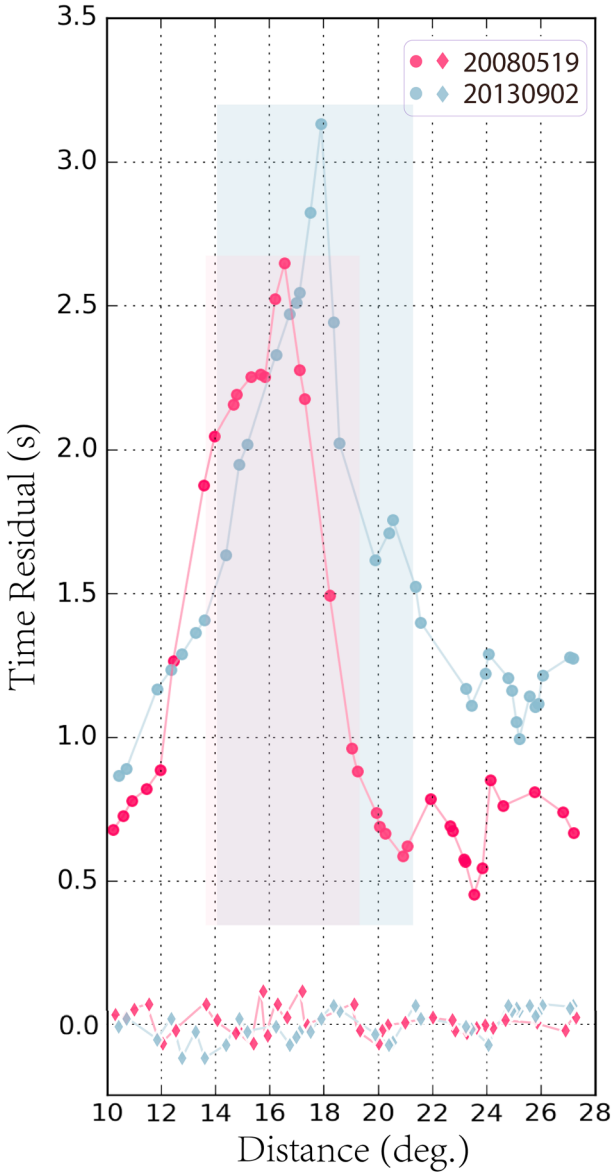

Figure 9. Time residuals of the first arrival between observations and the synthetics for the SH wave model obtained by using a scaling factor f = dlnVs/dlnVp = 1.5 from the preferred P velocity model for event 20080519 and event 20130902 (circle marker). The light red and blue region represent the records with a larger time lag (nearly twice than those outside), which is ~13°–18° for event 20080519 and 14°–19° for event 20130902. Time residual between observation and synthetics from our preferred SH wave model showed improved fitting results (diamond marker).

et al., 2013; Zhang et al., 2012) also reported a low S wave velocity layer in the MTZ with an average anomaly of −2%, broadly consistent with our results.

To explore the causes of high V_p/V_s ratio, we speculate two possible explanations of the chemical composition. Subducted slabs are generally composed of a thin oceanic crust layer underlain by a thicker residual harzburgite layer with olivine content and Mg/(Mg + Fe) value substantially higher than ambient mantle (Irifune et al., 2008). The presence of both layers will enhance P and SH wave velocities and thus cannot be responsible for the discrepancy between the variations of the two velocities observed in the MTZ beneath Northeast Asia. Major element effect such as increasing Fe content or decreasing Mg will decrease both V_p and V_s (Higo et al., 2006; Sinogeikin et al., 2001), although the amounts of velocity reductions are still debated (Mao et al., 2012; Schulze et al., 2018). A recent research (Thio et al., 2016) has listed three possible factors that could be responsible for an enhanced V_p/V_s and a decreased average velocity: (1) increased temperature environment. However, in our study region where the subducting slab is stagnant in the MTZ, the temperature should be lower than the ambient mantle; thus, increasing temperature cannot be an explanation. (2) Increased content of iron. Considering the response of V_p/V_s with respect to FeO content is relatively flat in their result; then the V_p/V_s value (1.88 on average) in the MTZ yielded in our study corresponds to a fairly large number of additional FeO content (>10 mol %, which we think is unacceptable) if we only consider the iron effect. This means that the variation of iron content has little effect in altering V_p/V_s and cannot be considered as a major reason. (3) Increased content of water. If we only consider the water effect, then the V_p/V_s value of 1.88 corresponds to ~1.8 wt % water (Thio et al., 2016), which we believe is in a reasonable range. Based on an observation of a low SH velocity layer and high V_p/V_s, Li et al. (2013) suggested a hydrated MTZ in this region according to the experiment by Jacobsen and Smyth (2006), who pointed out the velocity discordance between the compressional and shear wave on hydrous ringwoodite. The presence of water in the MTZ has also been revealed by petrological and other geophysical studies and predicted by mineral physics experiments (e.g., Fei et al., 2017; Houser, 2016; Mao et al., 2012; Pearson et al., 2014; Wang et al., 2017). If we attribute the ~2.7% increase of V_p/V_s ratio to the water effect alone, then the water content would be ~1.2–1.8 wt% in the MTZ beneath Northeast Asia based on the experimental data on iron-bearing wet ringwoodite (Jacobsen et al., 2004; Jacobsen & Smyth, 2006; Thio et al., 2016).

Except for the water effect, carbon-related melts migrated from the stagnant slab can also contribute to the low V_s in the MTZ. Experiments showed that carbonate may be subducted into the mantle and remain mobile in natural eclogites as part of a carbon recycle (Stagno et al., 2015). A recent study elucidated the existence of carbonated domains at the base of the MTZ from both geochemical and geophysical perspectives (Sun et al., 2017) and will induce incipient melting at that depth range (Dasgupta & Hirschmann, 2010). It was also suggested that upon reaching the melting condition, carbonic sediments lying above the slab will form diapirs at kilometer scales and rise through the whole MTZ either through the silicate matrix or the mobilized mantle rock (Ivanov & Litasov, 2014; Litasov et al., 2013). The presence of trace carbon-related melt may generate seismic low-V zones, amplify attenuation (Dasgupta & Hirschmann, 2010), and enhance V_p/V_s (Watanabe, 1993). This agrees with numerical simulations (Morra et al., 2015) that verified fluids from hydrous and carbon-bearing rocks ascending from the slab to the top of the transition zone, even if there are only small amounts of carbonates spaced within the subducted crust,

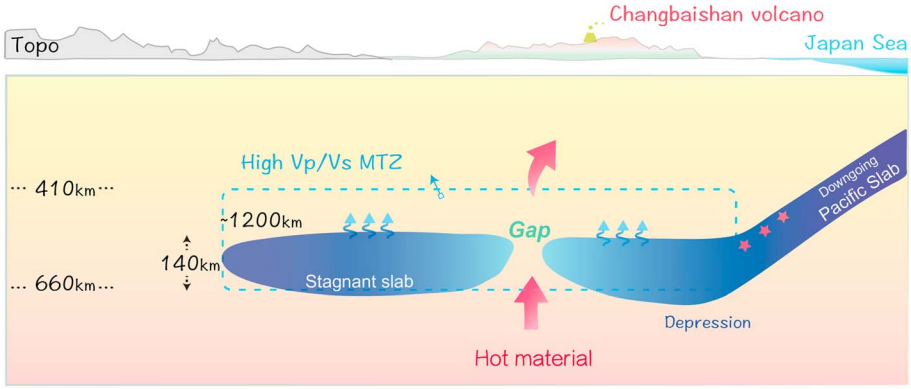

Figure 10. Schematic map showing the major features of the MTZ structure and the stagnant Pacific slab inferred from triplicated waveform modeling in this study. Red stars indicate the location of deep earthquakes occurred in the subducted slab.

they would collectively form large-scale melt diapirs that finally influence the seismic velocities. These studies suggest that a MTZ in which hydrated rocks and carbonates migrated from the stagnant slab could together cause a low *S* wave velocity; however, it is hard to distinguish their respective roles seismically. Through a double-diffusive mechanism (Richard et al., 2006), essentially 50–100% of the water in the slab is expelled into the transition zone for typical residence time ~50 Ma, during which in our case equilibrium is yet to be achieved.

In our suggested model, water- and/or carbon-related melts may have contributed to the observed low V_s and high V_p/V_s ratios in the MTZ of Northeast Asia. The estimated ~1.2wt% water by considering the water effect alone can be taken as the upper bound of water content in this region, which has not reached saturation. It is still challenging to constrain the respective abundance of water and carbon in the Earth's interior.

6.3. Low-*V* Anomaly in the Slab

A striking feature in our *P* and *S* wave velocity model is the presence of a low-*V* anomaly inside the stagnant slab, with −1% V_p and −3% V_s, respectively, compared to the IASP91 global model. The low-*V* anomaly has a width of ~150 km and lies mostly within the stagnant slab (Figure 5) at the west vicinity of the surface location of Changbaishan volcano (~124.5°E–~126°E, ~41.7°N–~43°N).

To understand the origin of Changbaishan volcano, Zhao et al. (2009) raised the “Big Mantle wedge” hypothesis to explain the evolution of the Cenozoic intraplate volcanism in Northeast Asia. The main idea is that hot and wet materials in the big mantle wedge above the stagnant Pacific slab lead to surface magmatism. Indeed, a low-*V* anomaly associated with these hot and wet materials has been revealed by many tomography studies; however, the vertical and horizontal extent of the low-*V* anomaly is under debate. A recent tomographic study by Tang et al. (2014) identified a low-*V* anomaly beneath the Changbaishan volcano that extends into the MTZ and penetrates through the stagnant slab, suggesting the deep origin of the volcanism. The existence of such a gap or low-*V* anomaly within the stagnant slab has been heatedly discussed and studied (e.g., Chen et al., 2017; Dokht et al., 2016; Guo et al., 2016; Liu et al., 2015; Ma et al., 2018). Chen et al. (2017) performed body wave tomography using travel time data from both local and regional earthquakes and teleseismic events. They did not observe such a low-*V* anomaly in the stagnant slab beneath the Changbaishan volcano. In Ma et al. (2018)'s 3-D *P* wave velocity model which was also constructed from arrival times of local, regional, and teleseismic events, the Changbaishan volcanic group was underlain by a low-*V* anomaly extending to the upper MTZ and a segmented stagnant slab in middle-lower MTZ. A gap in the stagnant slab beneath Changbaishan volcano was also imaged with limited resolution by using SS precursor data (Dokht et al., 2016), showing lower velocities than the adjacent slab but still higher velocities than the ambient mantle. Bearing with differences among all these studies, the general trend is that the low-*V* anomaly responsible for the surface volcano is believed to arise from a deeper depth in the MTZ or deeper, and the stagnant slab exhibit more complex features than previously thought.

In our research, we verified the existence of a low-V anomaly within the stagnant slab in the MTZ near the Changbaishan volcano through both P and SH triplicated waveform modeling for three deep events. The low-V anomaly imaged in this study has a similar location to the slab gap found by Tang et al. (2014). We propose that it may act as a conduit for hot deep mantle materials to penetrate through the thick slab and feed the surface Changbaishan volcano (Figure 10). The -1% V_p and -3% V_s of the low-V anomaly compared to IASP91 suggest a +200–+300 K temperature difference between the slab gap and ambient mantle, if we assume the temperature dependence of P and S wave velocity as -0.5×10^{-4} K^{-1} and -1×10^{-4} K^{-1}, respectively (Cammarano et al., 2003; Stixrude & Lithgow-Bertelloni, 2012).

The existence of such a low-V anomaly in the MTZ beneath Northeast Asia reflects the complexity of the slab structure and morphology and associated mantle processes, which is important for a comprehensive understanding of the subduction dynamics in this region. With the ongoing piling up and retreating of the trapped cold slab in the MTZ, the slab beneath Northeast Asia might be on the margin of instability (Li et al., 2015) and have developed some fractures or weak zones at the initial stage. The structural heterogeneity of the subducted slab, as imaged recently as the fracture zones beneath the Ulleung volcano (Liu et al., 2017; Zhao, 2009), may suggest that faults and weak zones within the slab could cause instability and vulnerability, further enabling buoyant mantle material upwelling to penetrate through the slab and eventually feed the surface volcanism. We speculated that the existence of such a slab gap in our model can be the manifestation of the original heterogeneity in the subducted slab, which may further speed up mantle avalanche as suggested by numerical simulations (Honda, Balachandar, et al., 1993; Honda, Yuen, et al., 1993), and eventually be precipitated by mantle upwelling emanated from the lower mantle.

7. Conclusion

By utilizing the 2-D triplicated waveform modeling technique, we have yielded a fine-scale velocity structure of the stagnant slab and the MTZ as a whole. Major results of this study are summarized as follows:

1. We showed a relative high-V layer with a thickness of 140 km and length of 1,200 km just atop the 660-km discontinuity in our profile beneath Northeast Asia. Taking this anomaly as the stagnant slab and considering the plate convergence rate of 7–10 cm/year in the western Pacific region, we deduce that the slab has a subducting age <30 Ma which denotes an Early Oligocene Pacific slab.
2. Based on the analysis of seismic velocity structure and geochemical studies, we suggested that both water- and carbon-related melts have contributed to a low V_s and high V_p/V_s MTZ revealed by P and SH triplicated waveform modeling.
3. The low-V anomaly within the stagnant slab is detected in our study. We believed that it may be the manifestation of the heterogeneity in the subducted slab and is a passage for hot deep mantle materials to penetrate through the thick slab and feed the surface Changbaishan volcano.

Acknowledgments
Waveform data for this study are provided by Data Management Centre of China National Seismic Network at Institute of Geophysics (http://www.seisdmc.ac.cn/, in Chinese; SEISDMC, doi:10.11998/SeisDmc/SN; Zheng et al., 2010), China Earthquake Networks Center and SN, SX, QH, NX, NM, GS, HB, HE, BJ, CC, BU, TJ, LN Seismic Networks, China Earthquake Administration. Thanks to Youcai Tang, Yoshio Fukao, Masayuki Obayashi, and Nathan Simmons for sharing their tomographic model. Discussions with Gaoshan Guo, Xu Wang, Tingting Yang, and Xiaozhuo Wei helped a lot in writing this paper. Ling Chen thanks COFFICE 422 at IGGCAS for the helpful discussions. We thank Computer Simulation Lab, IGGCAS, SeismoCluster in IGG, Nanjing University, and National Supercomputer Center in Guangzhou for the computing resources. GMT software (Wessel & Smith, 1998) and matplotlib (Hunter et al., 2007) were used in making part of the figures. We thank Editor Martha Savage and two anonymous reviewers for the constructive comments that helped to improve this paper. This research is supported by the National Natural Science Foundation of China (grant 41688103), the Strategic Priority Research Program of the Chinese Academy of Sciences (XDA20070302), and International Partnership Program of the Chinese Academy of Sciences (GJHZ1776). Zhongwen Zhan is partially supported by National Science Foundation grant 1722879.

References

Cammarano, F., Goes, S., Vacher, P., & Giardini, D. (2003). Inferring upper-mantle temperatures from seismic velocities. *Physics of the Earth and Planetary Interiors*, *138*(3-4), 197–222. https://doi.org/10.1016/S0031-9201(03)00156-0

Chen, C., Zhao, D., Tian, Y., Wu, S., Hasegawa, A., Lei, J., et al. (2017). Mantle transition zone, stagnant slab and intraplate volcanism in Northeast Asia. *Geophysical Journal International*, *209*(1), 68–85.

Chen, M., Tromp, J., Helmberger, D., & Kanamori, H. (2007). Waveform modeling of the slab beneath Japan. *Journal of Geophysical Research*, *112*, B02305. https://doi.org/10.1029/2006JB004394

Chen, Y. J., & Pei, S. (2010). Tomographic structure of East Asia: II. Stagnant slab above 660 km discontinuity and its geodynamic implications. *Earthquake Science*, *23*(6), 613–626. https://doi.org/10.1007/s11589-010-0760-4

Crotwell, H. P., Owens, T. J., & Ritsema, J. (1999). The TauP toolkit: Flexible seismic travel-time and ray-path utilities. *Seismological Research Letters*, *70*(2), 154–160. https://doi.org/10.1785/gssrl.70.2.154

Dasgupta, R., & Hirschmann, M. M. (2010). The deep carbon cycle and melting in Earth's interior. *Earth and Planetary Science Letters*, *298*(1–2), 1–13. https://doi.org/10.1016/j.epsl.2010.06.039

de Kool, M., Rawlinson, N., & Sambridge, M. (2006). A practical grid-based method for tracking multiple refraction and reflection phases in three-dimensional heterogeneous media. *Geophysical Journal International*, *167*(1), 253–270. https://doi.org/10.1111/j.1365-246X.2006.03078.x

Ding, X. Y., & Grand, S. P. (1994). Seismic structure of the deep Kurile subduction zone. *Journal of Geophysical Research*, *99*(B12), 23,767–23,786. https://doi.org/10.1029/94JB02130

Dokht, R. M., Gu, Y. J., & Sacchi, M. D. (2016). Waveform inversion of SS precursors: An investigation of the northwestern Pacific subduction zones and intraplate volcanoes in China. *Gondwana Research*, *40*, 77–90. https://doi.org/10.1016/j.gr.2016.07.006

Fei, H., Yamazaki, D., Sakurai, M., Miyajima, N., Ohfuji, H., Katsura, T., & Yamamoto, T. (2017). A nearly water-saturated mantle transition zone inferred from mineral viscosity. *Science Advances*, *3*(6), e1603024. https://doi.org/10.1126/sciadv.1603024

Fukao, Y. (1977). Upper mantle *P* structure on the ocean side of the Japan-Kurile arc. *Geophysical Journal International*, *50*(3), 621–642. https://doi.org/10.1111/j.1365-246X.1977.tb01338.x

Fukao, Y., & Obayashi, M. (2013). Subducted slabs stagnant above, penetrating through, and trapped below the 660 km discontinuity. *Journal of Geophysical Research: Solid Earth*, *118*, 5920–5938. https://doi.org/10.1002/2013JB010466

Fukao, Y., Obayashi, M., Inoue, H., & Nenbai, M. (1992). Subducting slabs stagnant in the mantle transition zone. *Journal of Geophysical Research*, *97*(B4), 4809–4822. https://doi.org/10.1029/91JB02749

Fukao, Y., Widiyantoro, S., & Obayashi, M. (2001). Stagnant slabs in the upper and lower mantle transition region. *Reviews of Geophysics*, *39*(3), 291–323. https://doi.org/10.1029/1999RG000068

Gorbatov, A., & Kennett, B. L. N. (2003). Joint bulk-sound and shear tomography for Western Pacific subduction zones. *Earth and Planetary Science Letters*, *210*(3-4), 527–543. https://doi.org/10.1016/S0012-821X(03)00165-1

Green, H. W. II, Chen, W. P., & Brudzinski, M. R. (2010). Seismic evidence of negligible water carried below 400-km depth in subducting lithosphere. *Nature*, *467*(7317), 828–831. https://doi.org/10.1038/nature09401

Guo, Z., Chen, Y. J., Ning, J., Yang, Y., Afonso, J. C., & Tang, Y. (2016). Seismic evidence of on-going sublithosphere upper mantle convection for intra plate volcanism in Northeast China. *Earth and Planetary Science Letters*, *433*, 31–43. https://doi.org/10.1016/j.epsl.2015.09.035

Hayes, G. P., Wald, D. J., & Johnson, R. L. (2012). Slab1.0: A three-dimensional model of global subduction zone geometries. *Journal of Geophysical Research*, *117*, B01302. https://doi.org/10.1029/2011JB008524

Higo, Y., Inoue, T., Li, B., Irifune, T., & Liebermann, R. C. (2006). The effect of iron on the elastic properties of ringwoodite at high pressure. *Physics of the Earth and Planetary Interiors*, *159*(3-4), 276–285. https://doi.org/10.1016/j.pepi.2006.08.004

Honda, S., Balachandar, S., Yuen, D. A., & Reuteler, D. (1993). Three-dimensional mantle dynamics with an endothermic phase transition. *Geophysical Research Letters*, *20*(3), 221–224. https://doi.org/10.1029/92GL02976

Honda, S., Yuen, D. A., Balachandar, S., & Reuteler, D. (1993). Three-dimensional instabilities of mantle convection with multiple phase transitions. *Science*, *259*(5099), 1308–1311. https://doi.org/10.1126/science.259.5099.1308

Houser, C. (2016). Global seismic data reveal little water in the mantle transition zone. *Earth and Planetary Science Letters*, *448*, 94–101. https://doi.org/10.1016/j.epsl.2016.04.018

Huang, J., & Zhao, D. (2006). High-resolution mantle tomography of China and surrounding regions. *Journal of Geophysical Research*, *111*, B09305. https://doi.org/10.1029/2005JB004066

Hunter, J. D. (2007). Matplotlib: A 2D graphics environment. *Computing in science & engineering*, *9*(3), 90–95.

Inoue, T. (1994). Effect of water on melting phase relations and melt composition in the system Mg_2SiO_4·$MgSiO_3$·H_2O up to 15 GPa. *Physics of the Earth and Planetary Interiors*, *85*(3–4), 237–263. https://doi.org/10.1016/0031-9201(94)90116-3

Irifune, T., Higo, Y., Inoue, T., Kono, Y., Ohfuji, H., & Funakoshi, K. (2008). Sound velocities of majorite garnet and the composition of the mantle transition region. *Nature*, *451*(7180), 814–817. https://doi.org/10.1038/nature06551

Ivanov, A. V., & Litasov, K. D. (2014). The deep water cycle and flood basalt volcanism. *International Geology Review*, *56*(1), 1–14. https://doi.org/10.1080/00206814.2013.817567

Jacobsen, S. D., & Smyth, J. R. (2006). Effect of water on the sound velocities of ringwoodite in the transition zone. In *Earth's Deep Water Cycle* (Vol. 168, p.131–145). Washington, DC: American Geophysical Union.

Jacobsen, S. D., Smyth, J. R., Spetzler, H., Holl, C. M., & Frost, D. J. (2004). Sound velocities and elastic constants of iron-bearing hydrous ringwoodite. *Physics of the Earth and Planetary Interiors*, *143-144*, 47–56. https://doi.org/10.1016/j.pepi.2003.07.019

Karato, S. I., & Jung, H. (2003). Effects of pressure on high-temperature dislocation creep in olivine. *Philosophical Magazine*, *83*(3), 401–414. https://doi.org/10.1080/0141861021000-025829

Kennett, B. L. N., & Engdahl, E. R. (1991). Travel times for global earthquake location and phase identification. *Geophysical Journal International*, *105*(2), 429–465. https://doi.org/10.1111/j.1365-246X.1991.tb06724.x

Kohlstedt, D. L., Keppler, H., & Rubie, D. C. (1996). Solubility of water in the α, β and γ phases of $(Mg, Fe)_2SiO_4$. *Contributions to Mineralogy and Petrology*, *123*(4), 345–357. https://doi.org/10.1007/s004100050161

Komatitsch, D., & Tromp, J. (2002a). Spectral-element simulations of global seismic wave propagation—I. Validation. *Geophysical Journal International*, *149*(2), 390–412. https://doi.org/10.1046/j.1365-246X.2002.01653.x

Komatitsch, D., & Tromp, J. (2002b). Spectral-element simulations of global seismic wave propagation—II. Three-dimensional models, oceans, rotation and self-gravitation. *Geophysical Journal International*, *150*(1), 303–318. https://doi.org/10.1046/j.1365-246X.2002.01716.x

Kuritani, T., Ohtani, E., & Kimura, J. I. (2011). Intensive hydration of the mantle transition zone beneath China caused by ancient slab stagnation. *Nature Geoscience*, *4*(10), 713–716. https://doi.org/10.1038/ngeo1250

Lei, J., & Zhao, D. (2005). P-wave tomography and origin of the Changbai intraplate volcano in Northeast Asia. *Tectonophysics*, *397*(3-4), 281–295. https://doi.org/10.1016/j.tecto.2004.12.009

Li, C., & van der Hilst, R. D. (2010). Structure of the upper mantle and transition zone beneath Southeast Asia from traveltime tomography. *Journal of Geophysical Research*, *115*, B07308. https://doi.org/10.1029/2009JB006882

Li, D., Helmberger, D., Clayton, R. W., & Sun, D. (2014). Global synthetic seismograms using a 2-D finite-difference method. *Geophysical Journal International*, *197*(2), 1166–1183. https://doi.org/10.1093/gji/ggu050

Li, J., Tosi, N., Maierová, P., & Yuen, D. A. (2015). Evidence from caustic waveform modeling for long slab thickening above the 660-km discontinuity under Northeast Asia: Dynamic implications. In *Subduction Dynamics: From Mantle Flow to Mega Disasters* (Vol. 211, pp. 5–18). Hoboken, NJ: John Wiley.

Li, J., Wang, X., Wang, X., & Yuen, D. A. (2013). P and SH velocity structure in the upper mantle beneath northeast China: Evidence for a stagnant slab in hydrous mantle transition zone. *Earth and Planetary Science Letters*, *367*, 71–81. https://doi.org/10.1016/j.epsl.2013.02.026

Li, J., & Yuen, D. (2014). Mid-mantle heterogeneities associated with Izanagi plate: Implications for regional mantle viscosity. *Earth and Planetary Science Letters*, *385*, 137–144. https://doi.org/10.1016/j.epsl.2013.10.042

Litasov, K. D., Shatskiy, A. N. T. O. N., & Ohtani, E. (2013). Earth's mantle melting in the presence of C–O–H-bearing fluid. In *Physics and Chemistry of the Deep Earth* (pp. 38–65). https://doi.org/10.1002/9781118529492.ch2

Liu, X., Zhao, D., Li, S., & Wei, W. (2017). Age of the subducting Pacific slab beneath East Asia and its geodynamic implications. *Earth and Planetary Science Letters*, *464*, 166–174. https://doi.org/10.1016/j.epsl.2017.02.024

Liu, Z., Niu, F., Chen, Y. J., Grand, S., Kawakatsu, H., Ning, J., et al. (2015). Receiver function images of the mantle transition zone beneath NE China: New constraints on intraplate volcanism, deep subduction and their potential link. *Earth and Planetary Science Letters*, *412*, 101–111. https://doi.org/10.1016/j.epsl.2014.12.019

Liu, Z., Park, J., & Karato, S. I. (2016). Seismological detection of low-velocity anomalies surrounding the mantle transition zone in Japan subduction zone. *Geophysical Research Letters*, *43*, 2480–2487. https://doi.org/10.1002/2015GL067097

Ma, J., Tian, Y., Liu, C., Zhao, D., Feng, X., & Zhu, H. (2018). *P*-wave tomography of Northeast Asia: Constraints on the Western Pacific plate subduction and mantle dynamics. *Physics of the Earth and Planetary Interiors*, *274*, 105–126. https://doi.org/10.1016/j.pepi.2017.11.003

Mao, Z., Lin, J. F., Jacobsen, S. D., Duffy, T. S., Chang, Y. Y., Smyth, J. R., et al. (2012). Sound velocities of hydrous ringwoodite to 16 GPa and 673 K. *Earth and Planetary Science Letters*, *331-332*, 112–119. https://doi.org/10.1016/j.epsl.2012.03.001

Mei, S., & Kohlstedt, D. L. (2000). Influence of water on plastic deformation of olivine aggregates: 1. Diffusion creep regime. *Journal of Geophysical Research*, *105*(B9), 21,457–21,469. https://doi.org/10.1029/2000JB900179

Morra, G., Yuen, D. A., Lee, S. M., & Zhang, S. (2015). Source of the Cenozoic Volcanism in Central Asia. In *Subduction Dynamics: From Mantle Flow to Mega Disasters* (Vol. 211, pp. 97–113). Washington, DC: American Geophysical Union.

Ohtani, E., Litasov, K., Hosoya, T., Kubo, T., & Kondo, T. (2004). Water transport into the deep mantle and formation of a hydrous transition zone. *Physics of the Earth and Planetary Interiors*, *143*, 255–269.

Okino, K., Ando, M., Kaneshima, S., & Hirahara, K. (1989). The horizontally lying slab. *Geophysical Research Letters*, *16*(9), 1059–1062. https://doi.org/10.1029/GL016i009p01059

Pearson, D. G., Brenker, F. E., Nestola, F., McNeill, J., Nasdala, L., Hutchison, M. T., et al. (2014). Hydrous mantle transition zone indicated by ringwoodite included within diamond. *Nature*, *507*(7491), 221–224. https://doi.org/10.1038/nature13080

Richard, G., Bercovici, D., & Karato, S. I. (2006). Slab dehydration in the Earth's mantle transition zone. *Earth and Planetary Science Letters*, *251*(1–2), 156–167. https://doi.org/10.1016/j.epsl.2006.09.006

Schmandt, B., Jacobsen, S. D., Becker, T. W., Liu, Z., & Dueker, K. G. (2014). Dehydration melting at the top of the lower mantle. *Science*, *344*(6189), 1265–1268. https://doi.org/10.1126/science.1253358

Schulze, K., Marquardt, H., Kawazoe, T., Boffa Ballaran, T., McCammon, C., Koch-Müller, M., et al. (2018). Seismically invisible water in Earth's transition zone? *Earth and Planetary Science Letters*, *498*, 9–16. https://doi.org/10.1016/j.epsl.2018.06.021

Si, S., Zheng, Y., Liu, B., & Tian, X. (2016). Structure of the mantle transition zone beneath the North China craton. *Journal of Asian Earth Sciences*, *116*, 69–80. https://doi.org/10.1016/j.jseaes.2015.11.006

Simmons, N. A., Myers, S. C., Johannesson, G., & Matzel, E. (2012). LLNL-G3Dv3: Global *P* wave tomography model for improved regional and teleseismic travel time prediction. *Journal of Geophysical Research*, *117*, B10302. https://doi.org/10.1029/2012JB009525

Sinogeikin, S. V., Bass, J. D., & Katsura, T. (2001). Single-crystal elasticity of γ-$(Mg_{0.91}Fe_{0.09})_2SiO_4$ to high pressures and to high temperatures. *Geophysical Research Letters*, *28*(22), 4335–4338. https://doi.org/10.1029/2001GL013843

Song, S. G., Zhang, L. F., Niu, Y., Wei, C. J., Liou, J. G., & Shu, G. M. (2007). Eclogite and carpholite-bearing metasedimentary rocks in the north Qilian suture zone, NW China: Implications for early Palaeozoic cold oceanic subduction and water transport into mantle. *Journal of Metamorphic Geology*, *25*(5), 547–563. https://doi.org/10.1111/j.1525-1314.2007.00713.x

Song, T.-R. A., Helmberger, D. V., & Grand, S. P. (2004). Low-velocity zone atop the 410-km seismic discontinuity in the northwestern United States. *Nature*, *427*(6974), 530–533. https://doi.org/10.1038/nature02231

Stagno, V., Frost, D. J., McCammon, C. A., Mohseni, H., & Fei, Y. (2015). The oxygen fugacity at which graphite or diamond forms from carbonate-bearing melts in eclogitic rocks. *Contributions to Mineralogy and Petrology*, *169*(2), 16. https://doi.org/10.1007/s00410-015-1111-1

Stixrude, L., & Lithgow-Bertelloni, C. (2012). Geophysics of chemical heterogeneity in the mantle. *Annual Review of Earth and Planetary Sciences*, *40*(1), 569–595. https://doi.org/10.1146/annurev.earth.36.031207.124244

Sun, W. D., Hawkesworth, C. J., Yao, C., Zhang, C. C., Huang, R. F., Liu, X., et al. (2017). Carbonated mantle domains at the base of the Earth's transition zone. *Chemical Geology*, *478*, 69–75. https://doi.org/10.1016/j.chemgeo.2017.08.001

Tajima, F., & Grand, S. P. (1995). Evidence of high velocity anomalies in the transition zone associated with southern Kurile subduction zone. *Geophysical Research Letters*, *22*(23), 3139–3142. https://doi.org/10.1029/95GL03314

Tajima, F., & Grand, S. P. (1998). Variation of transition zone high-velocity anomalies and depression of 660 km discontinuity associated with subduction zones from the southern Kuriles to Izu-Bonin and Ryukyu. *Journal of Geophysical Research*, *103*(B7), 15,015–15,036. https://doi.org/10.1029/98JB00752

Tajima, F., Katayama, I., & Nakagawa, T. (2009). Variable seismic structure near the 660 km discontinuity associated with stagnant slabs and geochemical implications. *Physics of the Earth and Planetary Interiors*, *172*(3-4), 183–198. https://doi.org/10.1016/j.pepi.2008.09.013

Takeuchi, N., Kawakatsu, H., Tanaka, S., Obayashi, M., Chen, Y. J., Ning, J., et al. (2014). Upper mantle tomography in the northwestern Pacific region using triplicated *P* waves. *Journal of Geophysical Research: Solid Earth*, *119*, 7667–7685. https://doi.org/10.1002/2014JB011161

Tang, Y., Obayashi, M., Niu, F., Grand, S. P., Chen, Y. J., Kawakatsu, H., et al. (2014). Changbai volcanism in Northeast China linked to subduction-induced mantle upwelling. *Nature Geoscience*, *7*(6), 470–475. https://doi.org/10.1038/ngeo2166

Tauzin, B., Kim, S., & Kennett, B. L. N. (2017). Pervasive seismic low-velocity zones within stagnant plates in the mantle transition zone: Thermal or compositional origin? *Earth and Planetary Science Letters*, *477*, 1–13. https://doi.org/10.1016/j.epsl.2017.08.006

Thio, V., Cobden, L., & Trampert, J. (2016). Seismic signature of a hydrous mantle transition zone. *Physics of the Earth and Planetary Interiors*, *250*, 46–63. https://doi.org/10.1016/j.pepi.2015.11.005

Tosi, N., Yuen, D. A., de Koker, N., & Wentzcovitch, R. M. (2013). Mantle dynamics with pressure- and temperature-dependent thermal expansivity and conductivity. *Physics of the Earth and Planetary Interiors*, *217*, 48–58. https://doi.org/10.1016/j.pepi.2013.02.004

Tschauner, O., Huang, S., Greenberg, E., Prakapenka, V. B., Ma, C., Rossman, G. R., et al. (2018). Ice-VII inclusions in diamonds: Evidence for aqueous fluid in Earth's deep mantle. *Science*, *359*(6380), 1136–1139. https://doi.org/10.1126/science.aao3030

van der Hilst, R., Engdahl, R., Spakman, W., & Nolet, G. (1991). Tomographic imaging of subducted lithosphere below northwest Pacific island arcs. *Nature*, *353*(6339), 37.

van der Hilst, R. D., Engdahl, E. R., & Spakman, W. (1993). Tomographic inversion of P and pP data for aspherical mantle structure below the northwest Pacific region. *Geophysical Journal International*, *15*(1), 264–302.

Wang, B., & Niu, F. (2010). A broad 660 km discontinuity beneath Northeast China revealed by dense regional seismic networks in China. *Journal of Geophysical Research*, *115*, B06308. https://doi.org/10.1029/2009JB006608

Wang, T., & Chen, L. (2009). Distinct velocity variations around the base of the upper mantle beneath Northeast Asia. *Physics of the Earth and Planetary Interiors*, *172*(3-4), 241–256. https://doi.org/10.1016/j.pepi.2008.09.021

Wang, T., Revenaugh, J., & Song, X. (2014). Two-dimensional/three-dimensional waveform modeling of subducting slab and transition zone beneath Northeast Asia. *Journal of Geophysical Research: Solid Earth*, *119*, 4766–4786. https://doi.org/10.1002/2014JB011058

Wang, X., Li, J., & Chen, Q.-F. (2017). Topography of the 410 km and 660 km discontinuities beneath the Japan Sea and adjacent regions by analysis of multiple-ScS waves. *Journal of Geophysical Research: Solid Earth*, *122*, 1264–1283. https://doi.org/10.1002/2016JB013357

Wang, Y., Wen, L., Weidner, D., & He, Y. (2006). SH velocity and compositional models near the 660-km discontinuity beneath South America and Northeast Asia. *Journal of Geophysical Research*, *111*, B07305. https://doi.org/10.1029/2005JB003849

Watanabe, T. (1993). Effects of water and melt on seismic velocities and their application to characterization of seismic reflectors. *Geophysical Research Letters*, *20*(24), 2933–2936. https://doi.org/10.1029/93GL03170

Wei, W., Xu, J., Zhao, D., & Shi, Y. (2012). East Asia mantle tomography: New insight into plate subduction and intraplate volcanism. *Journal of Asian Earth Sciences*, *60*, 88–103. https://doi.org/10.1016/j.jseaes.2012.08.001

Wessel, P., & Smith, W. H. (1998). New, improved version of Generic Mapping Tools released. *Eos, Transactions American Geophysical Union*, *79*(47), 579–579.

Ye, L., Li, J., Tseng, T. L., & Yao, Z. (2011). A stagnant slab in a water-bearing mantle transition zone beneath Northeast China: Implications from regional SH waveform modelling. *Geophysical Journal International*, *186*(2), 706–710. https://doi.org/10.1111/j.1365-246X.2011.05063.x

Yoshino, T., Manthilake, G., Matsuzaki, T., & Katsura, T. (2008). Dry mantle transition zone inferred from the conductivity of wadsleyite and ringwoodite. *Nature*, *451*(7176), 326–329. https://doi.org/10.1038/nature06427

Zhan, Z., Helmberger, D. V., & Li, D. (2014). Imaging subducted slab structure beneath the Sea of Okhotsk with teleseismic waveforms. *Physics of the Earth and Planetary Interiors*, *232*, 30–35. https://doi.org/10.1016/j.pepi.2014.03.008

Zhang, R., Wu, Q., Li, Y., & Romanowicz, B. (2012). Lateral variations in SH velocity structure of the transition zone beneath Korea and adjacent regions. *Journal of Geophysical Research*, *117*, B09315. https://doi.org/10.1029/2011JB008900

Zhao, D. (2009). Multiscale seismic tomography and mantle dynamics. *Gondwana Research*, *15*(3–4), 297–323. https://doi.org/10.1016/j.gr.2008.07.003

Zhao, D., Hasegawa, A., & Kanamori, H. (1994). Deep structure of Japan subduction zone as derived from local, regional, and teleseismic events. *Journal of Geophysical Research*, *99*(B11), 22,313–22,329. https://doi.org/10.1029/94JB01149

Zhao, D., Tian, Y., Lei, J., Liu, L., & Zheng, S. (2009). Seismic image and origin of the Changbai intraplate volcano in East Asia: Role of big mantle wedge above the stagnant Pacific slab. *Physics of the Earth and Planetary Interiors*, *173*(3-4), 197–206. https://doi.org/10.1016/j.pepi.2008.11.009

Zheng, X. F., Yao, Z. X., Liang, J. H., & Zheng, J. (2010). The role played and opportunities provided by IGP DMC of China National Seismic Network in Wenchuan earthquake disaster relief and researches. *Bulletin of the Seismological Society of America*, *100*(5B), 2866–2872. https://doi.org/10.1785/0120090257

Zhu, L., & Helmberger, D. V. (1996). Advancement in source estimation techniques using broadband regional seismograms. *Bulletin of the Seismological Society of America*, *86*(5), 1634–1641.